JOURNAL OF GEOPHYSICAL RESEARCH, VOL. 117, A12213, doi:10.1029/2012JA018175, 2012

Energetic particle injection, acceleration, and loss during the geomagnetic disturbances which upset Galaxy 15

Mark A. Clilverd,[1] Craig J. Rodger,[2] Donald Danskin,[3] Maria E. Usanova,[4] Tero Raita,[5] Thomas Ulich,[5] and Emma L. Spanswick[6]

Received 30 July 2012; revised 28 September 2012; accepted 17 October 2012; published 11 December 2012.

[1] On 5 April 2010 a series of energetic electron injections, acceleration, and loss events appeared to induce an operational anomaly in the Galaxy 15 geosynchronous communications satellite. We describe the energetic electron precipitation conditions leading to the anomaly. A few hours prior to the anomaly electron acceleration at >0.6 MeV, and loss at >30 keV, were observed simultaneously. The acceleration took place in the region of the Galaxy 15 satellite on the nightside and the precipitation of electrons primarily on the dayside. The precipitation was confined to *L*-shells outside of the plasmapause and appeared to be driven by chorus waves via a weak diffusion process. An hour prior to the anomaly, a solar wind shock event generated a few minutes of 30–150 keV electron precipitation but only on the dayside, over a large *L*-shell range ($4.8 < L < 13$). The timing of the precipitation burst was consistent with electromagnetic ion cyclotron (EMIC) waves seen on the dayside, but the high geomagnetic latitude of the precipitation suggests that EMIC wave growth associated with high cold density regions in the plasmasphere is unlikely to have played a role. A substorm injection event shortly after the shock appears to have ultimately triggered the upset on Galaxy 15. However, the peak >30 keV electron precipitation fluxes of 1.35×10^7 el cm^{-2} s^{-1} sr^{-1} were roughly the same level as other large substorm events previously analyzed, indicating either a sensitivity to the energetic electron environment prior to the event or that the satellite was in a vulnerable situation.

Citation: Clilverd, M. A., C. J. Rodger, D. Danskin, M. E. Usanova, T. Raita, T. Ulich, and E. L. Spanswick (2012), Energetic particle injection, acceleration, and loss during the geomagnetic disturbances which upset Galaxy 15, *J. Geophys. Res.*, *117*, A12213, doi:10.1029/2012JA018175.

1. Introduction

[2] On the 5 April 2010 a coronal mass ejection (CME) driven solar wind shock compressed the Earth's magnetosphere, and induced an operational anomaly in the Galaxy 15 geosynchronous communications satellite [*Allen*, 2010] which was close to MLT midnight at the time. The shock arrived at the Earth at 08:25 UT. Magnetospheric conditions following the compression have been comprehensively described by *Connors et al.* [2011]. Large dipolarisations were observed by THEMIS spacecraft in the midnight sector near $X = -11$, $Y = -2$ R_e, and a large flux transfer into the inner magnetosphere took place. The extreme geophysical conditions produced a substorm that began at 09:03 UT which appeared to induce the anomalies, and subsequent loss of control, in the Galaxy 15 geostationary communications satellite at 09:48 UT [*Connors et al.*, 2011]. We will therefore refer to this series of events as the Galaxy 15 period, made up of three event periods, the last of which is the Galaxy 15 substorm.

[3] During the Galaxy 15 substorm period several different processes could have produced energetic electron precipitation (EEP) into the atmosphere. One of these processes was the substorm itself, and although EEP is a well-known consequence of substorm occurrence in that clear signatures of substorms are often observed with riometer instruments [*Berkey et al.*, 1974; *Spanswick et al.*, 2009; *Clilverd et al.*, 2012], this particular substorm is worthy of investigation as an example of an extreme event. Another process that has previously been reported to generate electron precipitation into the atmosphere is the solar wind shock itself [e.g., *Clilverd et al.*, 2007]. Studies by *Zhou and Tsurutani* [1999] and *Tsurutani et al.* [2001] have suggested that the adiabatic

[1]British Antarctic Survey, Cambridge, UK.
[2]Department of Physics, University of Otago, Dunedin, New Zealand.
[3]Geomagnetic Laboratory, Natural Resources Canada, Ottawa, Ontario, Canada.
[4]Department of Physics, University of Alberta, Edmonton, Alberta, Canada.
[5]Sodankylä Geophysical Observatory, University of Oulu, Sodankylä, Finland.
[6]Department of Physics and Astronomy, University of Calgary, Calgary, Alberta, Canada.

Corresponding author: M. A. Clilverd, British Antarctic Survey, High Cross, Madingley Rd., Cambridge CB3 0ET, UK. (macl@bas.ac.uk)

compression can lead to a loss cone instability, wave growth and enhanced pitch angle scattering leading to EEP. The mechanism through which EEP could occur during the shock is unclear, but could include wave-particle interactions from electromagnetic ion cyclotron (EMIC) waves [*Fuselier et al.*, 2004], chorus waves [*Longden et al.*, 2008], or due to a compression-driven lowering of the mirror points of trapped particles to altitudes below ~100 km [*Spann et al.*, 1998]. EEP from EMIC waves has been reported by *Rodger et al.* [2008a] and *Miyoshi et al.* [2008] typically occurring on the evening side, close to the geomagnetic latitude of the plasmapause. Low-energy electron precipitation (~200 eV) by chorus waves has been associated with auroral forms [*Ni et al.*, 2011], and through theoretical studies of wave-particle interactions [*Horne*, 2002; *Horne et al.*, 2005]. The association of chorus wave with EEP is less certain.

[4] Understanding the occurrence, and driving mechanisms, of EEP into the atmosphere is an important requirement, both in determining the role of electron losses from the magnetosphere [*Reeves et al.*, 2003; *Clilverd et al.*, 2006; *Hendry et al.*, 2012], and the subsequent impact of EEP on the atmosphere [e.g., *Seppälä et al.*, 2007, 2009]. Further, the competing roles of electron acceleration and loss result in the complex response of the outer radiation belt to geomagnetic storms [*Reeves et al.*, 2003] and the consequent difficulty in providing accurate space weather predictions for the satellite industry [*Fok et al.*, 2008]. Electron losses into the atmosphere could reduce any hazard to satellites from electron acceleration processes or substorm injections, and identifying the characteristics of EEP could provide some information about loss mechanisms taking place. Furthermore, electron precipitation can be a signature of the acceleration processes taking place in the radiation belt, as the wave-particle interactions which accelerate some electrons also precipitate a large fraction [e.g., *Hendry et al.*, 2012]. Accurate measurements of EEP are difficult to make from spacecraft because the detectors either measure only a fraction of the bounce loss cone, or include some of the drift loss cone, or include some of the trapped component of the radiation belts [*Rodger et al.*, 2010a]. Ground-based measurements of EEP characteristics rely on monitoring the changes in D-region ionization caused by the precipitation [*Rodger et al.*, 2012]. These techniques effectively use the ionosphere as a large particle detector [*Clilverd et al.*, 2009], but only by using multi-instrument ground-based observations of the ionization produced by EEP is it possible to accurately characterize the EEP events.

[5] The enhanced ionization caused by EEP can produce odd nitrogen (NOx) and odd hydrogen (HOx) species in the upper and middle atmosphere [*Brasseur and Solomon*, 2005]. HOx is short-lived but responsible for the catalytic ozone loss at mesospheric altitudes [*Verronen et al.*, 2011], while NOx is much longer lasting in the absence of sunlight, and can be transported to lower altitudes where it can catalytically destroy ozone in the stratosphere, particularly at the poles [*Randall et al.*, 2005; *Seppälä et al.*, 2009]. Radiation belt processes can generate EEP for long periods, that is, up to ~10 d [*Rodger et al.*, 2010b; *Clilverd et al.*, 2010], and have been shown to generate EEP in large enough amounts to cause observable chemical changes in the upper atmosphere [*Verronen et al.*, 2011; *Andersson et al.*, 2012]. However, such extended periods of precipitation can be made up of several different class of event, with different characteristic energy spectra, MLT distributions, temporal variations, and fluxes. As such, it is important that the different driving mechanisms of EEP are understood in detail.

[6] *Connors et al.* [2011] noted that significant particle injections were observed during the Galaxy 15 substorm, but did not undertake any detailed descriptions. In this study we describe the energetic electron precipitation which occurred throughout the Galaxy 15 period using ground-based instrumentation, and relate it to electron detector measurements made at the same time by spacecraft, such as GOES and POES. We discuss in detail the energetic electron precipitation characteristics observed before the arrival of the solar wind shock event, during the shock itself, and as a result of the large substorm injection which occurred shortly after the shock. We compare the observations made over a range of magnetic local times, and discuss the driving mechanisms that might account for the energetic electron precipitation that occurred.

2. Geomagnetic Conditions

[7] The geomagnetic conditions during the Galaxy 15 period are summarized in Figure 1. The plot shows the solar wind parameters and geomagnetic indices from 00:00 to 12:00 UT on 5 April 2010. From top to bottom the panels show the variation of the solar wind speed and density, IMF Bz, and the AE and AO geomagnetic indices. The Bz panel indicates that predominantly negative Bz existed during most of the study period, with significant geomagnetic disturbance levels occurring after ~08:00 UT, including periods of large positive Bz. The ~09:00 UT substorm event was initiated by a sudden solar wind shock at ~08:25 UT shown by the sudden increase in solar wind speed and density, and highlighted by the dashed vertical line. The solar wind speed increased from an already high level of ~500 km s^{-1} to ~750 km s^{-1} at the time of the shock, with a simultaneous sixfold increase in solar wind density. These characteristics are consistent with the arrival of a solar wind stream interface. In all panels the time of the shock arrival at the Earth is indicated by the dashed vertical line.

[8] The geomagnetic indices AE and AO are plotted in the fourth panel of Figure 1. Variations in both indices show a large disturbance at 09:00 UT, but also some geomagnetic activity prior to the shock arrival, starting at ~04:30 UT and lasting until ~08:00 UT. The 04:30 UT disturbance levels are coincident with the period of negative Bz seen in the panel above. In summary, the CME-driven compressional shock that arrived at Earth at 08:25 UT produced severely disturbed geomagnetic conditions providing additional forcing to a magnetosphere that was already moderately disturbed, primarily by already high solar wind speeds, and recurring periods of negative Bz.

3. Experimental Setup

[9] This study combines ground-based and satellite observations of energetic electron fluxes or their influence on D-region ionization. On the ground we make use of riometer absorption measurements, broadband 0.5–10 kHz radio wave observations (VELOX), and very low frequency radio wave observations of man-made transmissions in the

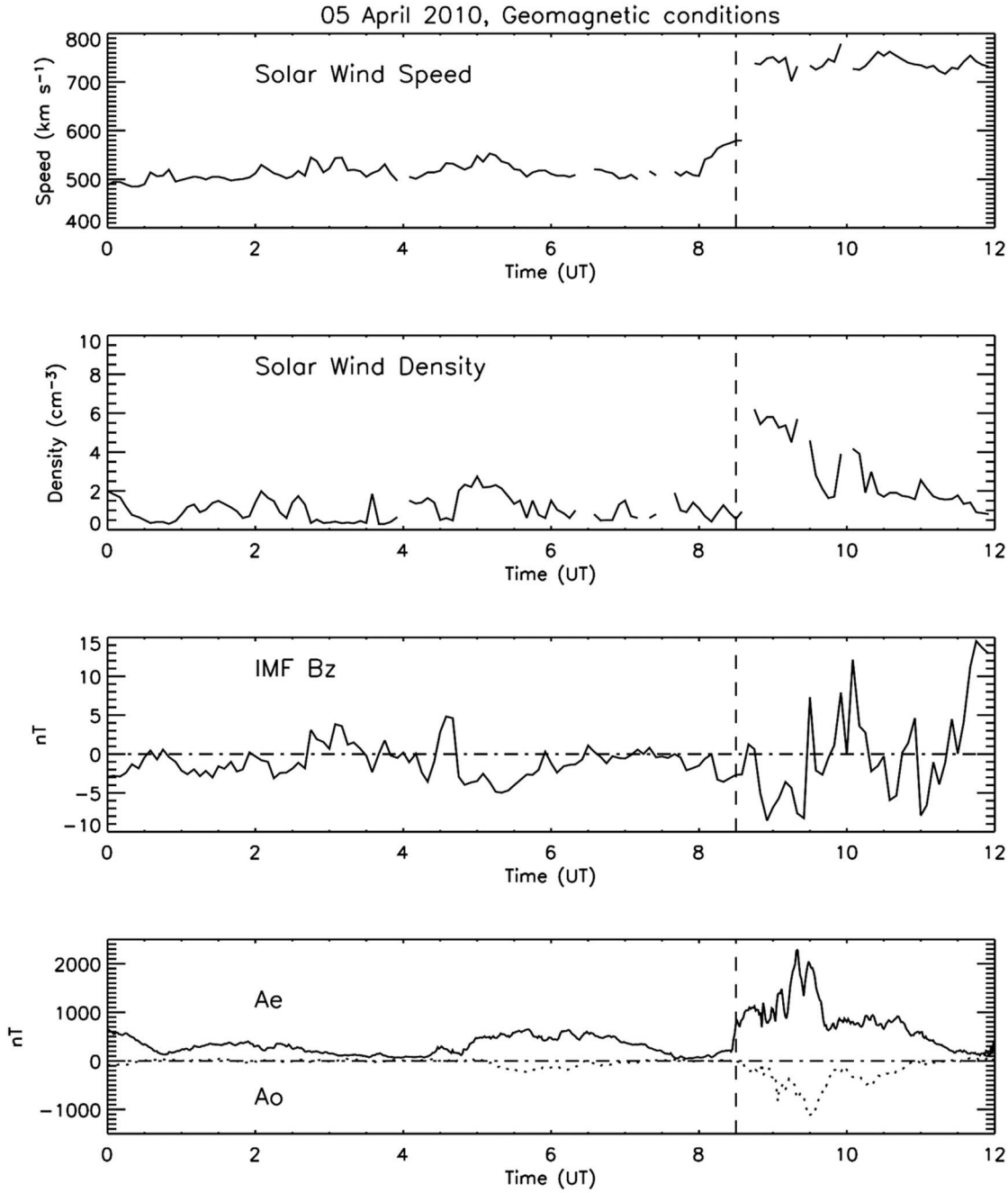

Figure 1. The geomagnetic conditions on 5 April 2010, 00:00–12:00 UT. From top to bottom the panels show the variation of the solar wind speed and density, the IMF Bz component, and the AE (positive values) and AO (negative values) geomagnetic index variations. The panels indicate that predominantly negative Bz existed during most of the study period, with moderate to severe geomagnetic disturbance levels occurring at ∼06:00 and ∼09:00 UT. The ∼09:00 UT disturbance was initiated by a sudden solar wind shock at ∼08:25 UT.

range 15–45 kHz (AARDDVARK). In space we make use of the GOES 11 electron detector, and all six of the POES satellites then operational, using both their parallel and field-aligned electron telescopes. Figure 2 shows the MLT distribution of the observations made at 06:00 UT and 09:00 UT on 5 April 2010, indicating the sites and satellite locations used in the analysis later in this study. On the 06:00 UT left-hand panel the Macquarie Island and Abisko riometer stations cover both the duskside and the dayside. VLF broadband wave data provided by the VELOX instrument comes from Halley close to MLT dawn. The GOES 11 satellite was in the MLT evening side, and the Galaxy 15 satellite was nearby [*Connors et al.*, 2011]. On the 09:00 UT right-hand panel the Macquarie Island and Dawson riometers are on the eveningside and midnightside, respectively, while Abisko is very close to MLT noon. The

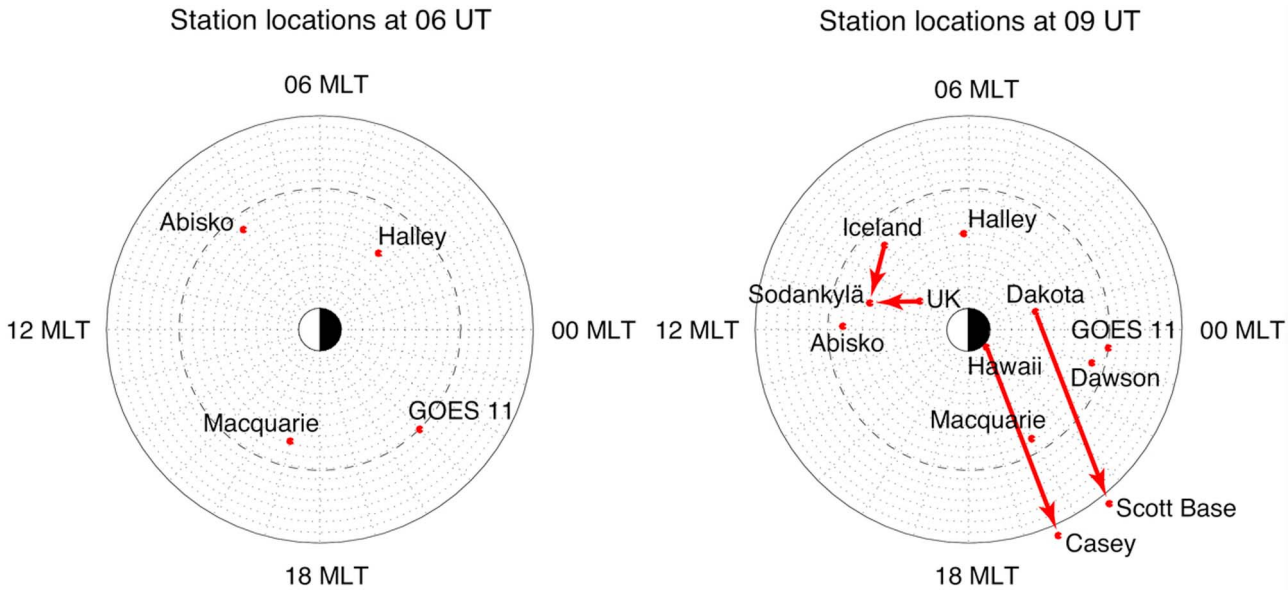

Figure 2. An indication of the MLT positions of the observation sites discussed in this study at 06:00 UT (left) and 09:00 UT (right) on 5 April 2010.

GOES 11 satellite was close to MLT midnight, with the Galaxy 15 satellite nearby. AARDDVARK data from subionospheric propagation paths indicated by the red lines linking transmitters to receivers (red dots) span the dayside using a receiver at Sodankylä, and the nightside using receivers at Scott Base and Casey in the Antarctic. Sodankylä also provides the pulsation magnetometer data used in this study, although it actually comes from a magnetometer at the same longitude but slightly further south, that is, Rovaniemi, Finland. POES data from the multiple satellite configuration is longitudinally averaged in order to provide 1 h timing resolution.

[10] The riometer data used in this study are provided from Macquarie Island (54.5°S, 158.9°E, L = 5.4), Dawson, Canada (64.05°N, 220.89°E, L = 6.0), and Abisko, Sweden (68.4°N, 18.9°E, L = 5.9). Riometers [*Little and Leinbach*, 1959] observe the integrated absorption of cosmic radio noise through the ionosphere, with increased absorption due to additional ionization, for example due to both proton and electron precipitation. Typically the riometer absorption is provided by a widebeam, 30 MHz, vertically pointing antenna. The dominant altitude of the absorption is typically in the range 70–100 km, that is, biased toward relatively soft particle energies (~30 keV electrons).

[11] The VELOX instrument (VLF/ELF Logger Experiment) is an experiment to record continuously, on a long-term basis, the VLF radio noise characteristics in 10 frequency bands between 0.5 and 9.3 kHz [*Smith*, 1995]. Located at Halley, Antarctica (75.5°S, 26.3°W, L = 4.5) the VELOX instrument is situated in an environment that is practically free from any man-made interference, and hence is ideally situated to monitor inner magnetospheric VLF wave activity close to the plasmapause, such as chorus and hiss in the 1–3 kHz range [*Rodger and Clilverd*, 2008b]. *Smith et al.* [2010] showed that chorus and hiss waves in the 1–3 kHz range were enhanced at Halley as a result of geomagnetically disturbed conditions (Kp > 2). The increase in amplitude with geomagnetic activity was typically 2–6 dB, and was usually observed over the period 05:00–15:00 UT (03:00–13:00 MLT) at all times of the year. Thus we would expect the Halley VELOX instrument to be in an ideal location to provide observations of VLF wave activity during the period under study in this analysis.

[12] AARDDVARK, the Antarctic-Arctic Radiation-belt Dynamic Deposition VLF Atmospheric Research Konsortia [*Clilverd et al.*, 2009] is a network of VLF receivers operating in the frequency range 10–50 kHz. Each receiver is capable of receiving narrowband transmissions from a number of powerful man-made communication transmitters, which can occasionally be as much as 15,000 km away. The AARDDVARK network uses narrow band subionospheric VLF/LF data to observe changes in the D-region ionization levels. This study makes use of the transmissions on the dayside from NRK (Iceland, 37.5 kHz, 64.2°N, 21.9°W, L = 5.57) and GVT (England, 22.1 kHz, 54.7°N, 2.9°W, L = 2.65) received at Sodankylä, Finland (67.4°N, 26.7°E, L = 5.34). The transmitter-receiver paths involved are ~1000 km long. On the nightside signals from NPM (Hawaii, 21.4 kHz, 21.4°N, 158.1°W, L = 1.17) and NDK (North Dakota, 25.2 kHz, 46.4°N, 98.3°W, L = 3.24) are examined that have been received at Casey, Antarctica (66.3°S, 110.5°E, L > 999) and Scott Base, Antarctica (77.8°S, 166.8°E, L > 32). The transmitter-receiver paths involved are ~7600 km and ~9400 km, respectively. The effects of changing propagation conditions in the mesosphere, often due to energetic particle precipitation, typically >50 keV during the night and >200 keV during the day, can be seen as either an increase or decrease in signal amplitude, and usually an increase in phase, depending on the modal mixture of each signal observed [*Barr et al.*, 2000; *Rodger et al.*, 2012]. Hence we can use the AARDDVARK data to indicate the presence of large-scale energetic particle precipitation regions.

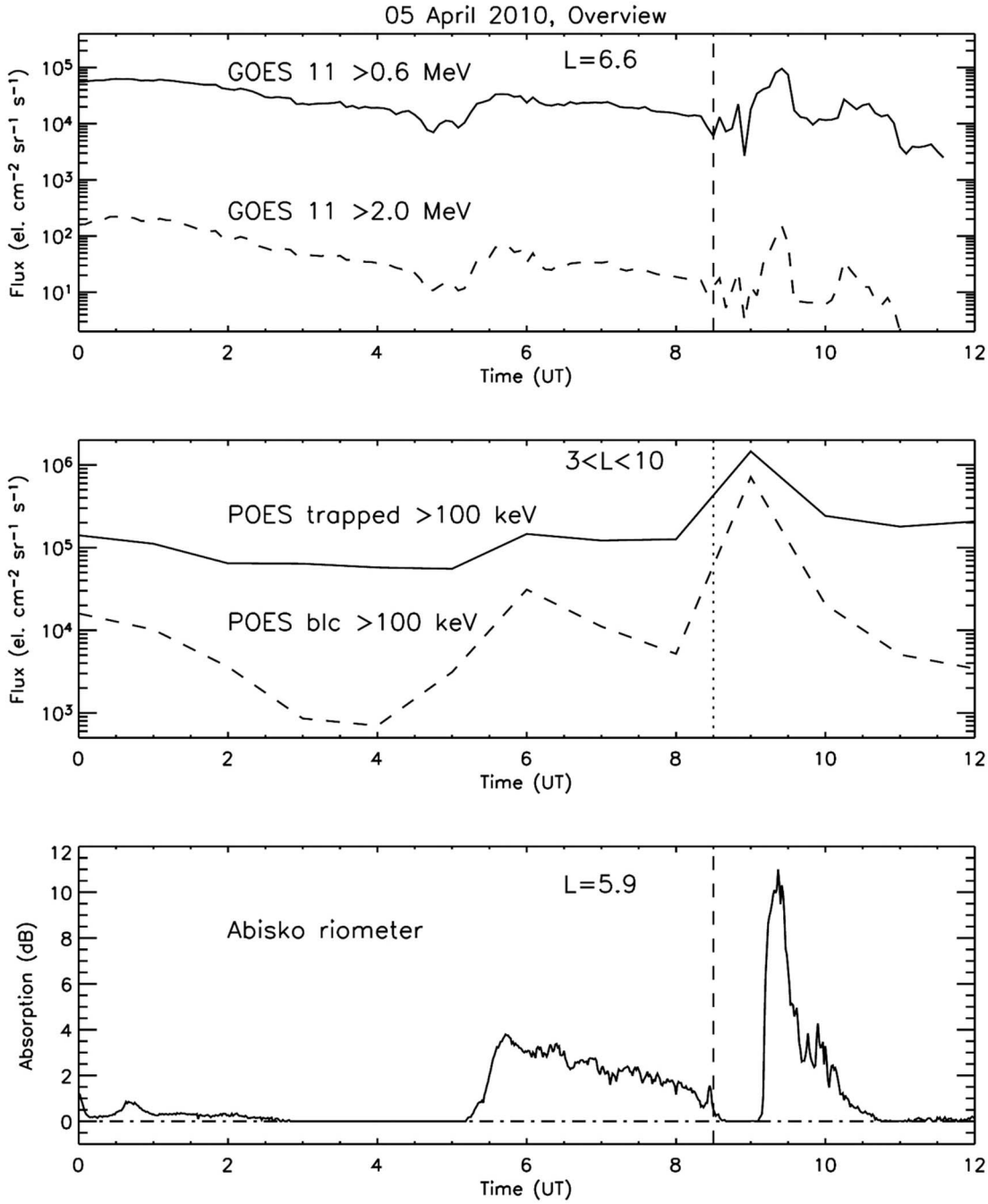

Figure 3. A plot indicating the satellite and ground-based observations that were made during the 00:00–12:00 UT period on 5 April 2010. Similarities can be seen in the variation of GOES 11 (>0.6 MeV and >2 MeV electrons), POES (>100 keV "trapped" and "bounce loss cone (blc)" electrons), and the Abisko riometer absorption at ∼06:00 and ∼09:00 UT.

[13] A latitudinal chain of pulsation magnetometers is located in Finland, and operated by the Sodankylä Geophysical Observatory. The magnetometers range from L = 3.4–6.1, and operate with a time resolution of 0.025 s. In this study we present magnetometer wave power over the frequency range 0.25–1.5 Hz from the Rovaniemi site, located at 66.8°N, 25.9°E, and at L = 5.1. Waves in this frequency range are known as Pc1–2 pulsations and are generated by the electromagnetic ion cyclotron (EMIC) instability near the magnetic equator. Pc1–2 waves propagate along the field line, and can also be observed on the ground [*Erlandson et al.*, 1996]. Solar wind compressions of the magnetosphere can generate Pc1 pulsations, as the compressions increase the ion anisotropy which, in turn, increases the EMIC wave growth rate [*Kangas et al.*, 1986].

[14] Geostationary (L = 6.6) electron flux data are provided by GOES 11 >600 keV and >2 MeV detectors [*Onsager et al.*, 1996]. At the time of this study GOES 11

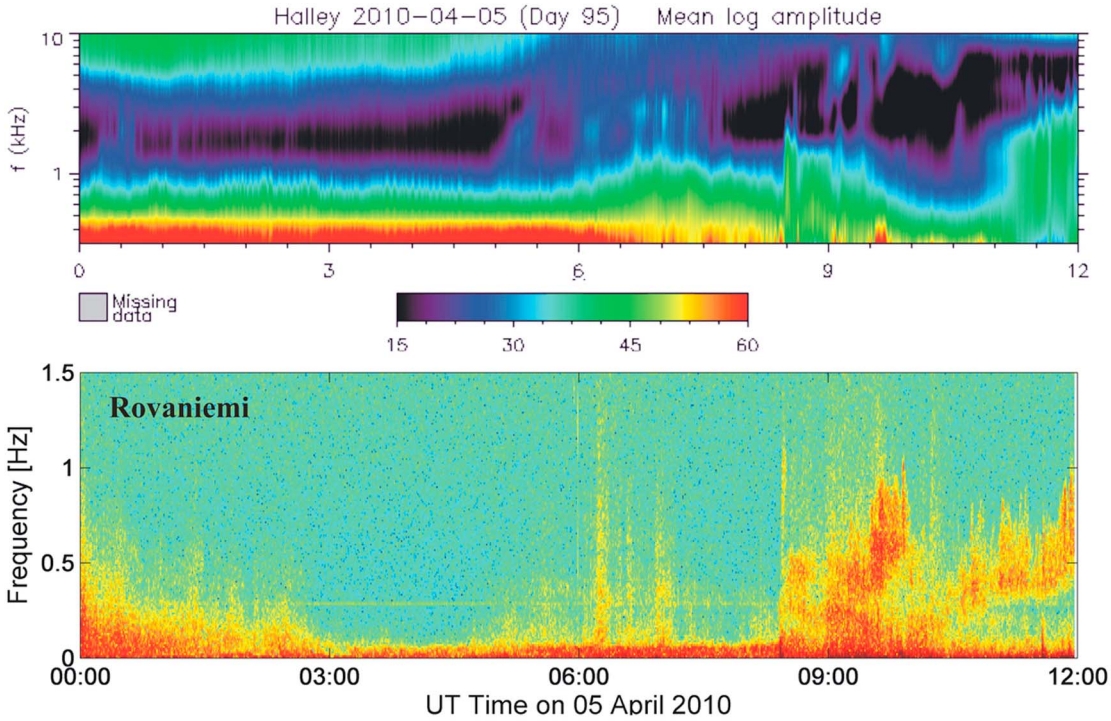

Figure 4. (top) The Halley VELOX data, 00:00–12:00 UT, 5 April 2010. VLF wave intensity from 0.5 to 10 kHz are shown (units of dB > 10^{-33} T^2 Hz^{-1}). The electron gyrofrequency (fce) at the *L*-shell of Halley is ∼10 kHz, corresponding to the top panel. Enhanced wave activity at ∼2 kHz can be observed at ∼05:00 UT, lasting until ∼08:00 UT, followed by a sudden enhancement at ∼1 kHz at 08:25 UT, as well as the appearance of ∼6 kHz waves at ∼09:00–10:00 UT. (bottom) The Rovaniemi Pc1–2 wave power over the same period. Electromagnetic ion cyclotron waves are observed following the solar wind compression at 08:25 UT.

was the primary SWPC satellite for the proton, electron, and magnetometer instruments, and was located at 135°W. The magnetic local time at 09:00 UT on 5 April 2010 (as shown in Figure 2) was 23:52 MLT, and thus the satellite was well positioned to observe the effects of substorm-injected energetic electrons. The GOES 11 D3 dome detector provides both the >600 keV and >2 MeV electron fluxes, primarily responding to trapped outer radiation belt particles. The relative variations of the electron fluxes observed at each energy channel are useful for scientific studies. We use the 5 min averaged GOES data which has been corrected for proton contamination, but also note that no solar proton event occurred during the study period, so proton contamination is likely to be minimal.

[15] We also make use of particle measurements by the Space Environment Monitor-2 (SEM-2) instrument package onboard the POES spacecraft which are in Sun-synchronous orbits at ∼800–850 km altitudes [*Evans and Greer*, 2004]. SEM-2 includes the Medium Energy Proton and Electron Detector (MEPED), in addition to the Total Energy Detector (TED). Together these instruments monitor electron fluxes from 50 eV up to 2700 keV. We make use of SEM-2 observations from up to 6 POES spacecraft. The SEM-2 detectors include integral electron telescopes with energies of >30 keV, >100 keV, and >300 keV, pointed in two directions.

[16] All POES data is available from http://poes.ngdc.noaa.gov/data/ with the full resolution data having 2 s time resolution. Analysis by *Rodger et al.* [2010a] indicated that the levels of contamination by comparatively low energy protons can be significant in the MEPED observations. As much as ∼42% of the 0° telescope >30 keV electron observations were typically found to be contaminated, although the situation was less marked for the 90° telescope (3.5%). However, NOAA has developed new techniques to remove the proton contamination from the POES SEM-2 electron observations, as described in Appendix A of *Lam et al.* [2010]. This algorithm is available for download through the Virtual Radiation Belt Observatory (ViRBO; http://virbo.org), and has been applied to the SEM-2 observations examined in our study. The 0°-pointing detectors are mounted on the three-axis stabilized POES spacecraft so that the center of each detector field of view is outward along the local zenith, parallel to the Earth-center-to-satellite radial vector. Another set of detectors, termed the 90° detectors are mounted approximately perpendicular to the 0° detector. In addition, there is also a set of omnidirectional measurements made from a dome detector which is mounted parallel to the 0° detectors. The detectors pointing in the 0° and 90° directions are ±15° wide, while the omnidirectional dome detectors (termed "omni") are ±60° wide. For the $3 < L < 10$ range we consider in this study the 90° detector appears to primarily respond to trapped electrons, and hence we will refer to it as the "trapped detector," while the 0° detector is responds to the electrons in the bounce loss cone, and is thus referred to as

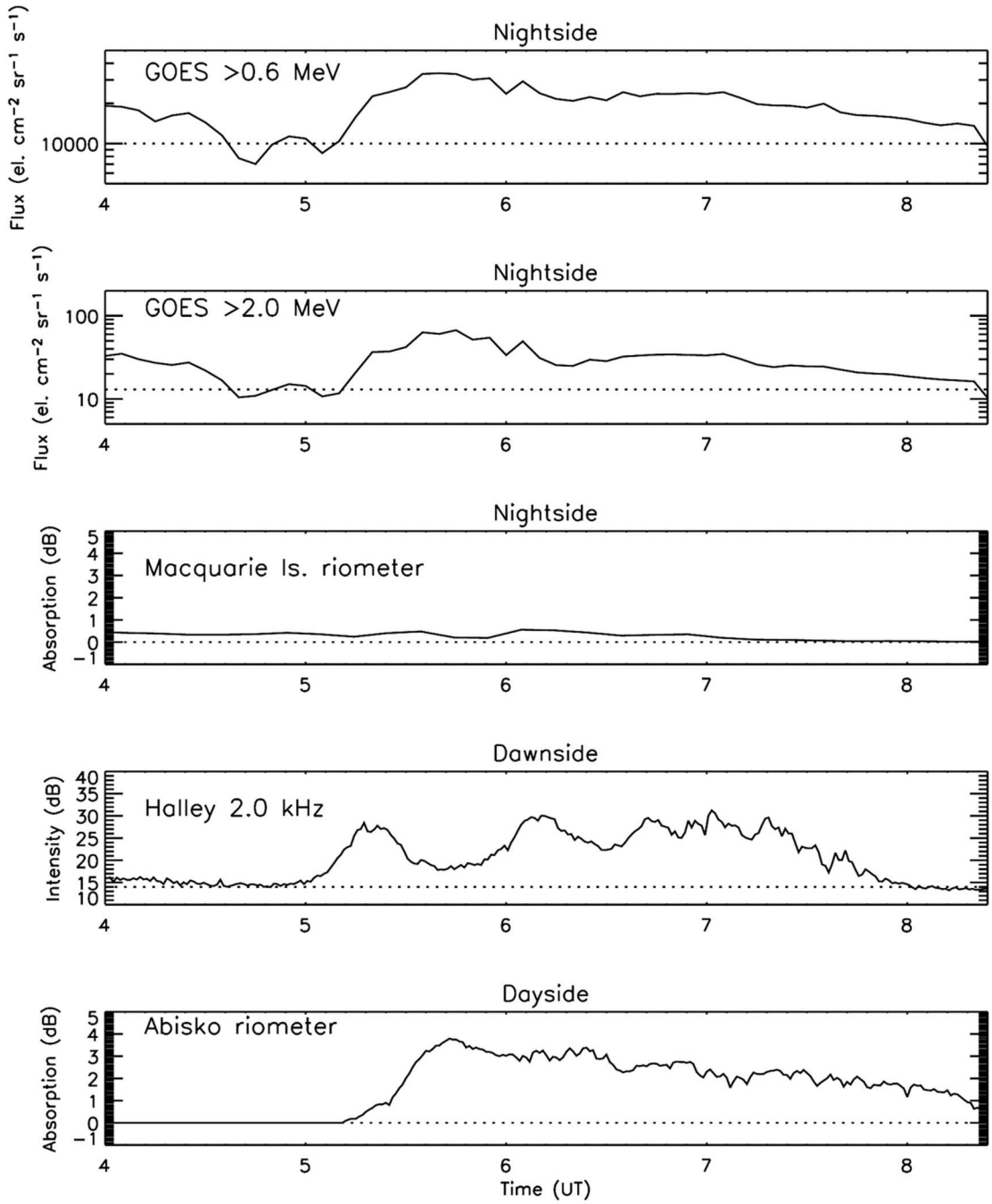

Figure 5. Observations during the period from 04:00–08:24 UT, with the upper two panels containing GOES >600 keV and >2 MeV fluxes, respectively. The two riometer panels show nightside Macquarie Island absorption, and dayside Abisko absorption variations, respectively, while the penultimate panel shows the dawnside VLF 2.0 kHz wave intensity at Halley, Antarctica.

the "blc detector" (see the modeling in the Appendix of *Rodger et al.* [2010c]).

4. Results

[17] The response of outer radiation belt energetic electron fluxes observed by satellites, and excess ionospheric ionization associated with electron precipitation into the atmosphere, from 00:00–12:00 UT on 5 April 2010 is shown in Figure 3. Figure 3 shows panels for the GOES 11 >0.6 MeV trapped electron flux at $L = 6.6$, the POES >100 keV trapped and blc electron flux at $3 < L < 10$, and the Abisko riometer absorption at $L = 5.9$. The time of the solar wind shock hitting the magnetosphere is identified by a vertical dashed line in all panels. GOES data represents nightside MLT conditions, POES data is zonally averaged in order to get 1 h time resolution, and the Abisko riometer data represents dayside MLT conditions.

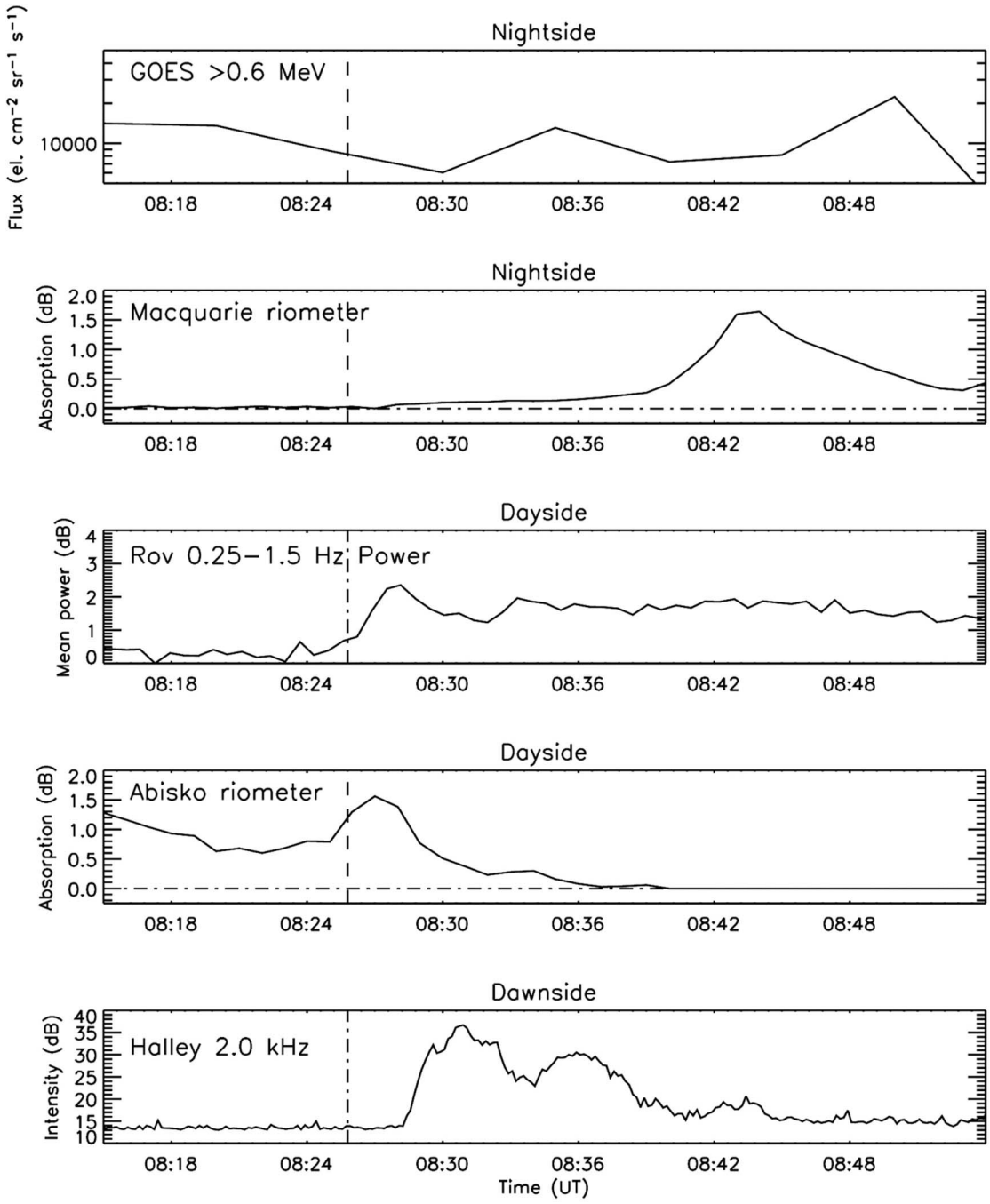

Figure 6. First to fifth panels: the GOES >600 keV fluxes, Macquarie Island riometer absorption, Rovaniemi Pc1–2 wave intensity, Abisko riometer absorption, and Halley VLF wave intensity from 08:15 to 08:54 UT. The time of the shock arrival is indicated by the vertical dashed line. The approximate MLT sector of the measurements is indicated for each panel.

[18] Three distinct features are apparent in Figure 3. The first is an increase in trapped fluxes at >600 keV and >100 keV at ~05:00 UT, as well as an increase in riometer absorption at the same time. This follows a small decrease in flux at 05:00 UT which maybe a result of a weak stretch and dipolarisation of the magnetic field on the nightside. The POES >100 keV blc electron flux also shows the same flux increase feature, and generally tracks the trapped flux variation throughout the study period, but with flux levels about a factor of 100 lower before the event and a factor of 5 lower during the event. A second feature is a small increase in riometer absorption at the time of the solar wind shock arrival, that is, 08:25 UT. This feature is not clearly seen in the satellite data. The third feature is a substantial increase in electron flux observed by satellite, and increased riometer absorption, at ~09:00 UT. This is coincident with the timing of the Galaxy 15 substorm.

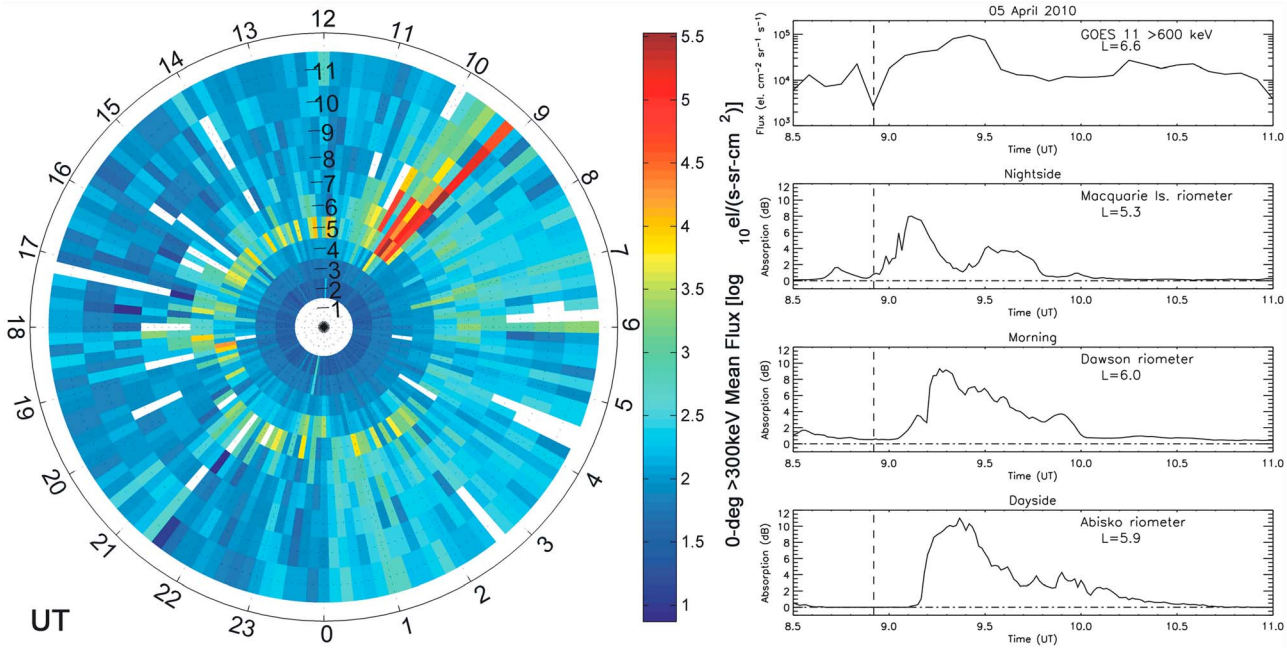

Figure 7. (left) The >300 keV blc flux as a function of UT and *L*-shell. The Galaxy 15 substorm can be seen as a sudden increase in flux just after 09:00 UT, spread over a large range of *L*-shell (L = 4–11). (right) The substorm impact on riometers on the nightside (Macquarie Island and Dawson) as well as on the dayside (Abisko). An approximate onset time of the substorm is indicated by the vertical dotted line at 08:55 UT.

[19] Whereas Figure 3 shows the energetic particle conditions during the period under study, Figure 4 shows some of the wave activity during the same period. The upper panel shows the 0.5–10 kHz VLF wave intensity recorded at Halley, Antarctica (L = 4.5), from 00:00 to 12:00 UT on 5 April 2010. Increases in VLF wave intensity in the 1–3 kHz range are observed from 05:00 to 08:00 UT, at ~08:30 UT, and in the 4–6 kHz range at ~09:00 UT. These periods coincide with the particle features identified in Figure 3. Enhancements in VLF wave activity have been associated with wave-particle interactions, driving energetic electron acceleration, and loss [*Horne et al.*, 2005]. In the lower panel the Pc1–2 wave power from Rovaniemi, Finland (L = 5.1), is shown. Impulsive, nonstructured, noise can be seen at 00:00 UT, and ~06:00 UT, with EMIC-like wave structures occurring at about 0.5 Hz from ~08:30 UT. In sections 4.1–4.3 we discuss each of these features in turn, describing their principle characteristics and potential driving mechanisms.

4.1. Wave-Induced Acceleration and Precipitation (03:00–08:00 UT)

[20] Prior to the arrival of the solar wind shock at 08:25 UT there was a period of weak geomagnetic disturbance, as exhibited by AE, which began at 04:30 UT and remained elevated until ~07:00 UT. This geomagnetic disturbance appears to be driven by negative IMF Bz conditions, with extreme values of ~−5 nT. An apparent consequence of the geomagnetic disturbance is a period of enhanced trapped fluxes observed by the GOES detectors on the nightside. Figure 5 shows the period from 04:00–08:24 UT, with the first and second panels containing GOES >600 keV and >2 MeV fluxes, respectively. The two riometer panels show nightside Macqaurie Island absorption, and dayside Abisko absorption variations, respectively, while the penultimate panel shows the dawnside VLF 2.0 kHz wave intensity at Halley, Antarctica. Typically a factor of 4 increase in trapped flux is observed at >600 keV and >2 MeV, with a slow recovery lasting about 3 h in the GOES data. The VLF waves show a 15 dB increase in intensity at the start of the event, before declining to pre-event levels by ~08:00 UT. The two riometer panels showing nightside Macqaurie Island absorption and dayside Abisko absorption variations are set to the same absorption scale. The nightside riometer observes no enhancement in absorption associated with EEP during the period when dayside absorption is increased.

4.2. Compression-Induced Precipitation (08:25 UT)

[21] At 08:25 UT on 5 April 2010 a solar wind shock arrived at the Earth's magnetosphere, and initiated a period of geomagnetic disturbance. In Figure 3 the summary plot of this study period showed that there was an almost immediate response to the arrival of the shock, as was seen by the ~1 dB enhancement in dayside riometer absorption. In Figure 6 we zoom in on the period close to the shock arrival time, plotting GOES >600 keV fluxes, Macquarie Island riometer, Abisko riometer absorption, Rovaniemi Pc1–2 wave intensity, and Halley VLF wave intensity from 08:15 to 08:54 UT. The time of the shock arrival is indicated by the vertical dashed line. The Abisko riometer panel clearly shows enhanced dayside riometer absorption immediately following the shock arrival which adds to the declining absorption event associated with the chorus wave activity reported in section 4.1, and peaks at 08:26 UT. Extended analysis of

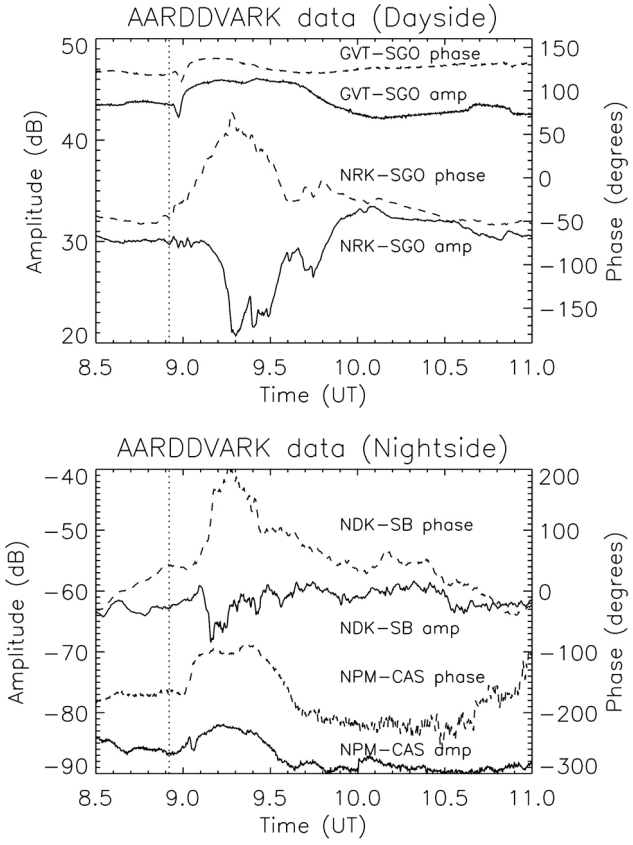

Figure 8. (top) AARDDVARK data received at Sodankylä during 5 May 2010, Iceland-Sodankylä (NRK-SGO, 37.5 kHz, $L \sim 5$–6), and UK-Sodankylä (GVT-SGO, 22.1 kHz, $2.5 < L < 5.3$). Both phase (dashed lines) and amplitude (solid line) are shown for each transmitter-receiver path, with the approximate substorm onset time shown by a vertical dotted line. (bottom) AARDDVARK data from two transmitters received at Antarctic stations on the nightside, Hawaii-Casey (NPM-CAS, 21.4 kHz, $1 < L < 999$), and North Dakota-Scott Base (NDK-SB, 25.2 kHz, $1 < L < 32$).

the Finnish riometer chain suggests that the riometer signal associated with the shock is observed over a large latitude range (from Hornsund in Svalbard at $L = 13$, to Rovaneimi in Finland at $L = 5.1$, that is, from the uppermost station to midway down the chain, but not at the most equatorward riometers).

[22] On the nightside Figure 6 shows that no clear variation is observed by the GOES >600 keV electron detectors at the time of the shock (>2 MeV not shown, but no clear variation), while the Macquarie Island riometer is similarly unresponsive at 08:25 UT. The Macquarie riometer absorption does increase after 08:40 UT, which is coincident with the time of a small substorm reported by *Connors et al.* [2011].

[23] Some of the dayside response to the shock is apparent in Figure 6 through the enhancement of VLF wave intensity at 2.0 kHz at Halley ($L = 4.5$), and the onset of EMIC wave activity at Rovaniemi in Finland ($L = 5.1$). VLF wave activity increased in the range 1.0–2.0 kHz, but was delayed by 5 min relative to the onset time of the shock. The EMIC wave activity is seen to onset at 08:25 UT at ~0.5 Hz, with a peak of wave power at 08:27 UT, continuing until about 10:00 UT and gradually increasing in frequency to ~1 Hz. This is consistent with the characteristics of an IPDP (intervals of pulsations of diminishing periods) EMIC wave structure which have previously been associated with relativistic electron precipitation near the plasmapause [*Rodger et al.*, 2008a].

4.3. Substorm Injection and Precipitation (08:30–11:00 UT)

[24] The geophysical conditions following the shock event produced a substorm that began at 09:03 UT [*Connors et al.*, 2011]. The substorm appeared to induce the anomalies, and subsequent loss of control, in the Galaxy 15 satellite, and therefore the energetic electron precipitation of this particular substorm is worthy of investigation as an example of an extreme event. Figure 7 shows the POES-observed >300 keV blc flux as a function of UT and L-shell (left panel) for the day of 5 April 2010. The substorm can be seen as a sudden increase in flux just after 09:00 UT, spread over a large range of L-shells ($L = 4$–11). The fluxes increased from typically 2×10^2 el cm^{-2} s^{-1} sr^{-1} to 4×10^5 el cm^{-2} s^{-1} sr^{-1} with peak values at $L \sim 7$, and factors of 10 × lower precipitating fluxes ±2 L-shells either side of the peak. In the >30 keV detector the equivalent peak fluxes were 2×10^7 el cm^{-2} s^{-1} sr^{-1} at $L = 7$, and 1×10^7 el cm^{-2} s^{-1} sr^{-1} at $L = 6$. Figure 7 (right) shows the substorm impact on riometers on the nightside (Macquarie Island and Dawson) as well as on the dayside (Abisko). An approximate onset time of the increase in absorption at Macquarie Island is indicated by the vertical dotted line at 08:55 UT. Nighttime absorption levels due to the substorm peaked at 09:07 UT and 6–8 dB, with a second smaller peak about 30 min later. On the dayside the riometer absorption was ~11 dB, and also showed a double peaked structure, but overall the absorption event was delayed by 15 min relative to the nightside. The increased absorption on the dayside compared with the nightside is consistent with the enhanced response of a riometer in daylight [*Rodger et al.*, 2012], and the delay of the onset of the substorm precipitation from nightside to dayside (12:00 MLT to near 00:00 MLT in 15 min) is consistent with the drift period of ~300 keV electrons at $L = 6$. The timing of the second peak 30 min after the first in all of the riometers is also consistent with the drift period of ~300 keV electrons at $L = 6$, suggesting that the electron precipitation region drifted around the Earth more than once. Figure 7 (right) also shows the variation of GOES 11 >600 keV flux during the event (>2 MeV flux not shown, but exhibited similar variations). Trapped fluxes increased by a factor of ~20 and GOES observations indicate that electrons with energies >2 MeV were injected during the substorm.

[25] The substorm also produced well defined effects on VLF radio propagation conditions, both on the nightside and the dayside. Figure 8 (top) shows AARDDVARK data received at Sodankylä using signals from two transmitters on the dayside, Iceland-Sodankylä (NRK-SGO, 37.5 kHz, $L \sim 5$–6), and UK-Sodankylä (GVT-SGO, 22.1 kHz, $2.5 < L < 5.3$). Both phase (dashed lines) and amplitude

(solid line) are shown for each transmitter-receiver path, with the same time of onset as Figure 7 shown as a vertical dotted line (08:55 UT). The lower panel shows AARDDVARK data from two transmitters received at Antarctic stations on the nightside, Hawaii-Casey (NPM-CAS, 21 4 kHz, $1 < L < 999$), and North Dakota–Scott Base (NDK-SB, 25.2 kHz, $1 < L < 32$). Both of the transmitter-receiver paths on the nightside cross the geomagnetic equator, are very long, and only part of the path is influenced by the substorm precipitation. As a result they are quite complicated to analyze. However, we can see that in all four paths the phase increases during the substorm, with changes in the order of 100°, and the amplitude shows either increases or decreases. This behavior is consistent with previous observations of substorm effects on narrowband radio wave signals [*Clilverd et al.*, 2012, and references therein]. Only the NRK-SGO path, which is a quasi-constant *L*-shell path near $L = 6$, shows a double peak pattern in both phase and amplitude, with the initial peak occurring at ~09:18 UT, followed by the second smaller peak about 30 min later. The temporal variation in the NRK-SGO phase and amplitude is similar to that observed in the riometer data, whereas the other paths with greater geomagnetic latitude range do not show any obvious response at the time of the second peak, suggesting that the precipitation associated with the second peak is constrained in latitude, and centered on $L \sim 6$.

5. Discussion

5.1. Wave-Induced Acceleration and Precipitation (03:00–08:00 UT)

[26] *Horne et al.* [2005] and *Xiao et al.* [2010, and references therein] suggest that wave-particle interactions between seed population electrons and chorus waves can provide an acceleration mechanism that enhances the fluxes of relativistic electrons, particularly those at ~1 MeV. Superluminous waves (Auroral Kilometric Radiation) could also produce the stochastic acceleration of electrons [*Xiao et al.*, 2007] if those waves are present in the radiation belts under appropriate conditions. In particular, *Xiao et al.* [2012] have found that Z-mode waves can yield rapid acceleration of radiation belt electrons. In Figures 4 and 5 our observations during the 04:00–08:00 UT event suggest that 1–3 kHz chorus waves are present and enhanced, at least on the dawnside. In the MLT wave pattern cartoon developed by *Summers et al.* [1998], and shown as Figure 7 in that paper, the influence of chorus waves on wave-particle interactions covers the MLT region from somewhat before midnight, through the dawnside, to near midday. Thus the presence of chorus waves on the dawnside is consistent with the observation of enhanced electron fluxes in GOES 11 at midnight as a result of wave-induced electron acceleration.

[27] In addition to electron acceleration occurring on the nightside and dawnside, Figure 5 also shows that electron precipitation occurred in this period on the dayside but not on the nightside. The Abisko riometer showed a maximum of 4 dB of absorption during the wave-induced acceleration event, peaking just before 06:00 UT, and slowly declining until ~08:00 UT. The temporal variation is very similar to the behavior of the GOES 11 trapped electron fluxes. In contrast, the duskside Macquarie Island riometer, showed very little variation in absorption during this period, suggesting that no energetic electron precipitation was occurring in that MLT region. This is also consistent with the suggestion that chorus waves are capable of inducing electron precipitation, and that the dusk-nighttime location of Macquarie Island at this time is outside of the longitude of the anticipated chorus-electron interaction region, presumably because of the lack, or weak intensity, of any chorus waves that may be present in that region [*Summers et al.*, 1998; *Horne*, 2002]. Inspection of the Finnish riometer chain data for this event [http://www.sgo.fi/Data/Riometer/rioData.php] suggests that the dayside electron precipitation did not occur below $L = 4.5$, that is, was confined outside of the plasmapause, and this is also consistent with the Summers chorus interaction region cartoon where the plasmapause defines the inner boundary of the chorus region. The POES >100 keV blc electron fluxes shown in Figure 3 indicate a factor of 40 increase in flux from the time just before the start of the event to the maximum during the event. The >300 keV blc fluxes (not shown) increased by a factor of 2–3 at the same time, although the observed pre-event flux levels were at the detector noise floor, so it is unclear exactly what factor increase occurred at these higher energies. However, we can ask a simple question at this stage: are the POES blc fluxes observed large enough to account for the 4 dB increase in absorption? Here we can calculate the electron energy spectrum (30 keV–2.5 MeV) using the different POES energy channels, and as in the work of *Clilverd et al.* [2008, 2012] we can use a simple ionospheric model to describe the balance of electron number density, N_e, in the lower ionosphere, based on that given by *Rodger et al.* [1998], and further described by *Rodger et al.* [2007, 2012]. By calculating height-integrated differential absorption using the method described by *Rodger et al.* [2012], we can estimate the riometer absorption generated by the observed POES energetic electron precipitation fluxes.

[28] Using the POES integral blc fluxes we calculate that the best fit for the e-folding energy of the precipitating electron spectrum is 55 keV. The POES blc flux levels, extrapolated to a spectrum that ranges from 30 keV–3 MeV, give an Abisko riometer absorption level of 0.5 dB, assuming daytime conditions and the underlying ionosphere above Abisko taken from the International Reference Ionosphere [*Rodger et al.*, 2012]. This is considerably smaller than observed, and we estimate that we would need to increase the >30 keV blc flux from 5.7×10^4 el cm^{-2} s^{-1} sr^{-1} observed by POES to 1.7×10^6 el cm^{-2} s^{-1} sr^{-1} in order to reproduce the Abisko 3.5 dB absorption levels shown in Figure 5. That equates to a factor of 30 multiplication in POES blc fluxes in order to reproduce the observations. This is consistent with the idea that the POES blc detector is only seeing part of the blc at geomagnetic latitudes associated with the outer radiation belt, and that some adjustment needs to be made to the POES blc fluxes to take into account the orientation of the telescope to the blc, and the distribution of electrons within the blc [*Hendry et al.*, 2012]. Of course we have only made a rough calculation using the POES data, and more comprehensive studies are needed which compensate for the use of zonal and meridional averaged POES data in this study.

5.2. Compression-Induced Precipitation (08:25 UT)

[29] At the time of the solar wind compression of the dayside magnetosphere dayside riometer absorption was observed almost immediately. There are several competing mechanisms by which such a rapid response could occur. The high compression of the magnetopause and the outer magnetosphere during the solar wind shock could drive particle precipitation due to lowering of the mirror points of trapped particles to altitudes below ~100 km [*Spann et al.*, 1998]. *Zhou and Tsurutani* [1999] and *Tsurutani et al.* [2001] suggested that the adiabatic compression could lead to a loss cone instability, wave growth, and enhanced pitch angle scattering. *Zhou et al.* [2003], using FAST and DSMP auroral imaging, showed that the precipitation of 1–10 keV electrons was highly isotropic, filling the loss cone, and was likely driven by adiabatic compression. *Fuselier et al.* [2004] proposed that the scattering and precipitation of ~50 keV protons immediately following a large solar wind shock was due to interactions with electromagnetic ion cyclotron (EMIC) waves. This assumption was later confirmed by *Usanova et al.* [2010] who observed EMIC-related precipitation of 30–80 keV protons on the NOAA POES satellites during enhanced solar wind dynamic pressure. *Longden et al.* [2008] presented observations of riometer absorption following solar wind shocks, and suggested that enhancements in VLF chorus waves as the driving mechanism.

[30] In this study we have presented both EMIC and VLF chorus wave data during the solar wind shock. The EMIC wave enhancement occurred near simultaneously with the increase in riometer absorption, whereas the VLF chorus wave enhancement occurred about 5 min later. However, the chorus observations were made on the dawnside and the riometer absorption observations were made at noon (MLT). *Zhou and Tsurutani* [1999] found that shock-induced aurora brighten away from MLT noon at speeds of 6–11 km s^{-1}. This suggests that the delay time of shock effects from noon to dawn could be in the order of 10 min, but this is still a factor of 2 longer than observed with the Halley VLF chorus data.

[31] Conversely the EMIC wave enhancements were made near MLT noon, and showed no significant delay compared with the riometer absorption. However, the riometer absorption signature was observed from $4.8 < L < 13$, which is inconsistent with the EMIC-driven precipitation mechanism as this is generally believed to be restricted to inside the plasmapause, requiring interactions between hot ring current protons and cold plasmaspheric ions to give rise to EMIC wave growth [*Fuselier et al.*, 2004]. Precipitating protons with energies of ~50 keV are unlikely to trigger any response in riometer absorption as they generate excess ionization at altitudes above at which riometers are sensitive [*Turunen et al.*, 2009; *Rodger et al.*, 2012].

[32] The riometer response suggests electron precipitation with energies of >30 keV, and the lack of any observed response in VLF AARDDVARK data (not shown) suggests electron energies <150 keV. Electron precipitation through the modification of high-latitude dayside EMIC waves [*Usanova et al.*, 2008] is a potential mechanism, as the probability of observing EMIC waves in space increases during magnetospheric compressions. *Anderson et al.* [1992] suggested that the EMIC growth rate peaks at two locations, including at high dayside L-shells ($5 < L < 11$) where the geomagnetic field is relatively weak as well inside the plasmapause where the cold plasma density is high. Theoretical study by *Summers et al.* [1998] suggests that EMIC waves can interact with MeV electrons via Doppler-shifted cyclotron resonance and cause their precipitation into the atmosphere. This interaction is possible in extended regions of high plasma density (like plasmaspheric plumes) but is unlikely to affect 30–150 keV electrons. So far, no confirmed electron precipitation associated with these high L-shell dayside EMIC waves has been reported and the electron energy range is unexpectedly low.

5.3. Substorm Injection and Precipitation (08:30–11:00 UT)

[33] *Clilverd et al.* [2008, 2012] combined riometer absorption data and AARDDVARK radio wave data to estimate the electron precipitation flux occurring during substorms. We undertake the same calculation here, using the dayside riometer observations from Abisko (11.5 dB), and the daytime phase and amplitude perturbations: +105°/−9 dB for NRK-SGO, and +12°/+2 dB for GVT-SGO. The energetic electron precipitation produces mesospheric ionization, and its effects on VLF wave propagation can be modeled using the Long Wave Propagation Code (LWPC) [*Ferguson and Snyder*, 1990]. LWPC models VLF signal propagation from any point on Earth to any other point. Given electron density profile parameters for the upper boundary conditions, LWPC calculates the expected amplitude and phase of the VLF signal at the reception point. A more detailed description of this technique can be found in the work of *Clilverd et al.* [2008].

[34] Using POES blc flux observations we can calculate the best fit for an energy spectrum e-folding energy in much the same way as in section 4.3. POES suggests that at the peak of the substorm precipitation the spectrum can be represented by an e-folding energy of 70 keV. The e-folding energy compares well with the spectra shown in Figure 6 of *Clilverd et al.* [2008]. By using the e-folding energy spectrum value, and sweeping through a range of flux levels, we can determine the most likely precipitating flux that will give the same results as the observations. In this case using the riometer absorption target of 11.5 dB we calculate that the substorm >30 keV flux was 8.6×10^6 el cm^{-2} s^{-1} sr^{-1}. The >30 keV flux level is about the same as the large substorms reported by *Rodger et al.* [2012] who remodeled the substorm fluxes of *Clilverd et al.* [2008, 2012], and slightly less than the flux reported by POES for the same energy range (2×10^7 el cm^{-2} s^{-1} sr^{-1} at $L = 7$, and 1×10^7 el cm^{-2} s^{-1} sr^{-1} at $L = 6$) in this event.

[35] However, when using the e-folding spectrum and the flux required to model the riometer observations we found that we were unable to reproduce the changes in the VLF propagation conditions, particularly the Iceland-Sodankylä path (NRK-SGO) using the LPWC. This path is quasi-constant at $L = 5$–6, and should be representative of the center of the precipitation region during the substorm [*Berkey et al.*, 1974]. *Clilverd et al.* [2008] found that they required a non e-folding spectrum to accurately model VLF propagation conditions, and instead used spectral information from the LANL-97A geostationary satellite which showed much higher fluxes at higher energies than a typical 50 keV

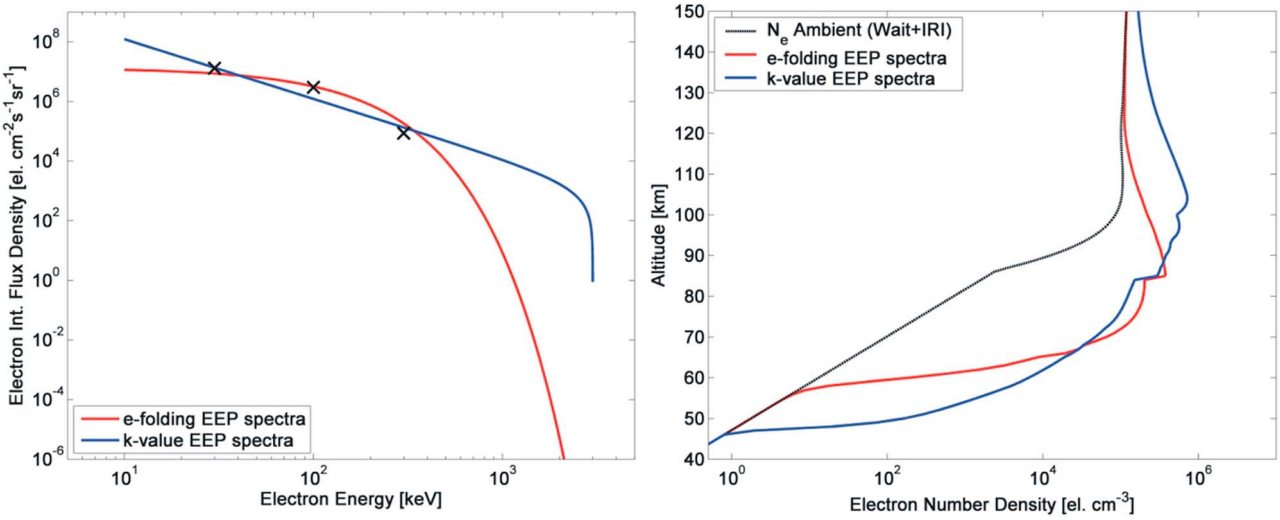

Figure 9. (left) Electron integral flux density varying with electron energy over the range 10 keV to 3 MeV for a 70 keV e-folding spectra (red line) and a $k = -3$ power law spectra (blue line). The black crosses represent the >30, >100, >300 keV blc fluxes measured by POES at the peak of the substorm. (right) The calculated altitude-dependent electron number density as a result of precipitating electrons with the two spectra. The solid black line represents the nondisturbed ionosphere during daytime in the region of Abisko in April 2010. The ambient ionospheric profile is determined using a Wait nighttime profile up to 85 km and an International Reference Ionosphere profile above; see text for more details.

e-folding spectrum would suggest, particularly at energies >400 keV (see Figure 6 of that study). In the work of *Clilverd et al.* [2010] a fit was made to DEMETER electron spectra from ~90–700 keV in terms of a power law where the slope (scaling exponent, k) typically ranged from −1 to −3. A power law slope of $k = -3$ represents the LANL-97A substorm spectra in the work of *Clilverd et al.* [2008], and in our current study is able to reproduce both the VLF propagation changes shown by NRK-SGO during the 09:00 UT substorm, and the peak riometer absorption value of 11.5 dB, using a >30 keV flux of 1.35×10^7 el cm^{-2} s^{-1} sr^{-1}. This >30 keV EEP flux magnitude value is similar to the e-folding flux, and similar to the >30 keV blc flux levels observed by POES. In contrast with the 05:00–08:00 UT wave-driven event discussed in section 5.1, there is no difference in the experimentally estimated flux and the POES-observed blc fluxes, whereas the wave-driven event suggested a factor of ~30 difference. This could be explained by different pitch angle distributions within the blc, driven by strong or weak diffusion for the various processes. Strong diffusion would be more likely to isotropically fill the loss cone, and produce a smaller conversion factor for the POES observations. Thus we suggest that substorms have pitch angle distribution that is consistent with an isotropically filled loss cone, while the wave-driven precipitation event has the characteristics of a weak diffusion process [*Kennel and Petschek*, 1966].

[36] Figure 9 shows the similarities and differences of the 70 keV e-folding spectrum (red lines) and the $k = -3$ spectrum (blue lines) which both reproduce the Abisko-reported riometer absorptions. The left-hand panel shows how the electron integral flux density varies with electron energy over the range 10 keV to 3 MeV. The black crosses represent the >30, >100, >300 keV blc fluxes measured by POES at the peak of the substorm. It is clear that using POES data alone, the spectrum can be well represented by either e-folding, or power law characteristics but there are only three energy ranges to constrain the spectral fitting. Both spectra give the same riometer absorption value, and only the addition of the AARDDVARK observations and modeling can differentiate between the two. *Xiao et al.* [2008, and references therein] showed that fits to the energy spectrum of trapped electron measurements from the LANL satellites are best described by a kappa-type (KT) power law index. In the energy range considered in this study the kappa-type distributions shown in the work of *Xiao et al.* [2008] closely resemble our $k = -3$ spectral gradient and lend weight to the use of a power law energy spectrum to model the EEP events. The right-hand panel shows the calculated altitude-dependent electron number density as a result of precipitating electrons with the two different spectra. The solid black line represents the nondisturbed ionosphere during daytime in the region of Abisko in April 2010. The ambient ionospheric profile is determined using a Wait nighttime profile up to 85 km, and an IRI profile above [after *Rodger et al.*, 2012]. Although the >30 keV flux is similar for both spectra, the $k = -3$ line shows higher fluxes >500 keV, and the 70 keV e-folding line shows higher fluxes for ~100–300 keV. The effect on the ionosphere when these spectra precipitate is for greater ionization at low altitudes (~50 km) and at high altitudes (~100 km) for the $k = -3$ spectra, while the 70 keV e-folding spectra produces higher electron number density at ~70 km. This altitude difference can be significant in terms of chemical changes caused by the ionization, the lifetime of the species produced, and their impact on the neutral atmosphere [*Brasseur and Solomon*, 2005].

6. Summary

[37] On 5 April 2010 a CME-driven solar wind shock compressed the Earth's magnetosphere, and induced an

operational anomaly in the Galaxy 15 geosynchronous communications satellite [*Allen*, 2010]. The shock arrived at the Earth at 08:25 UT. In this study we have described the energetic electron precipitation throughout the Galaxy 15 period, including the characteristics observed before the arrival of the solar wind shock event, during the shock itself, and as a result of the large substorm injection shortly after the shock.

[38] Prior to the solar wind shock a period of negative IMF Bz gave rise to a period of geomagnetic disturbance during which electron acceleration occurred, consistent with the presence of chorus waves that were observed on the dawnside. Electron acceleration and loss was observed at the same time, with the precipitation of electrons into the atmosphere occurring primarily on the dayside of the Earth. Using POES integral blc fluxes for >30, >100, and >300 keV we calculate that the e-folding energy of the precipitating electron spectrum to be 55 keV, with peak fluxes of 1.7×10^6 el cm^{-2} s^{-1} sr^{-1} in order to reproduce the Abisko 3.5 dB absorption observed. The dayside energetic electron precipitation, identified by riometer absorption enhancements, was confined to L-shells outside of the plasmapause, which is consistent with the likely inner boundary of the chorus region. Although the POES blc >100 keV fluxes increased by a factor of 40 during the event, the calculated fluxes on the basis of the ground-based observations were a factor of 30 times larger again. This is consistent with the idea that some adjustment needs to be made to the POES blc fluxes to take into account the orientation of the telescope to the blc, and the nonisotropic distribution of electrons within the blc. The observations suggest that the chorus-wave event produced energetic electron precipitation via a weak diffusion process.

[39] During the solar wind shock, a few minutes of 30–150 keV electron precipitation was observed on the dayside, and over a large L-shell range ($4.8 < L < 13$). The timing of the pulse was consistent with the enhancement of EMIC waves in the range 0.25–1 Hz on the dayside, whereas enhanced VLF chorus waves were only observed 5 min later. Adiabatic magnetospheric compression leading to loss cone instability, wave growth, and enhanced pitch angle scattering is likely to have taken place, but the low energy of precipitating electrons and the high geomagnetic latitude of the precipitation suggests that interaction with EMIC waves in high cold density regions is unlikely to have played a role. High-latitude dayside EMIC waves may have caused the enhanced pitch angle scattering, but further work is required to identify the mechanism conclusively.

[40] The electron precipitation fluxes driven by the substorm injection occurring shortly after the shock arrival were estimated using riometer and AARDDVARK subionospheric VLF wave propagation observations. Riometer absorption levels of ~11 dB during the substorm represent an extreme event, although the estimated fluxes were roughly the same level as other large substrom events previously analyzed. The >30 keV fluxes were found to be 1.35×10^7 el cm^{-2} s^{-1} sr^{-1} which was consistent with those observed by the POES blc telescopes, and suggest an isotropically filled blc. However, using POES to estimate the energy spectrum of the substorm-driven electron precipitation gave an e-folding energy spectrum of 70 keV, but the observed AARDDVARK responses suggest that an e-folding energy spectrum would underestimate the higher (>400 keV) electron fluxes. Instead, a power law spectrum is more appropriate, with a scaling factor of $k = -3$.

[41] In summary, a few hours prior to the Galaxy 15 anomaly electron acceleration at >0.6 MeV, took place in the region of the Galaxy 15 satellite on the nightside. Then, an hour prior to the anomaly, a solar wind shock event generated a few minutes of 30–150 keV electron precipitation, possibly associated with EMIC waves, but was observed only on the dayside over a large L-shell range ($4.8 < L < 13$). Finally, a substorm injection event was triggered by the shock, and appears to have ultimately triggered the upset on Galaxy 15. However, we have shown that the peak >30 keV electron precipitation fluxes of 1.35×10^7 el cm^{-2} s^{-1} sr^{-1} were only about the same level as other large substorm events previously analyzed, indicating either a sensitivity to the energetic electron environment prior to the event, or that the satellite was in a vulnerable situation.

[42] **Acknowledgments.** The authors would like to acknowledge the support of the Australian Antarctic Division project ASAC 1324 for the Casey data. We would also like to acknowledge the use of the AAD data system for the provision of the Macquarie Island Riometer data, http://www.ips.gov.au/World_Data_Centre/1/8. The Scott Base experiment is supported by Antarctica New Zealand, event K060. M.U. is funded by the Canadian Space Agency. The research leading to these results has received funding from theEuropean Union Seventh Framework Programme (FP7/2007–2013) under grantagreement n°263218. C.J.R. was supported by the New Zealand Marsden Fund.

[43] Masaki Fujimoto thanks the reviewers for their assistance in evaluating this paper.

References

Allen, J. (2010), The Galaxy 15 anomaly: Another satellite in the wrong place at a critical time, *Space Weather*, *8*, S06008, doi:10.1029/2010SW000588.

Anderson, B. J., R. E. Erlandson, and L. J. Zanetti (1992), A statistical study of Pc 1–2 magnetic pulsations in the equatorial magnetosphere: 1. Equatorial occurrence distribution, *J. Geophys. Res.*, *97*, 3075–3088, doi:10.1029/91JA02706.

Andersson, M., P. T. Verronen, S. Wang, C. J. Rodger, M. A. Clilverd, and B. R. Carson (2012), Precipitating radiation belt electrons and the production of mesospheric hydroxyl during 2004–2009, *J. Geophys. Res.*, *117*, D09304, doi:10.1029/2011JD017246.

Barr, R., D. L. Jones, and C. J. Rodger (2000), ELF and VLF radio waves, *J. Atmos. Sol. Terr. Phys.*, *62*, 1689–1718, doi:10.1016/S1364-6826(00)00121-8.

Berkey, F. T., V. M. Driatskiy, K. Henriksen, B. Hultqvist, D. H. Jelly, T. I. Shchuka, A. Theander, and J. Yliniemi (1974), A synoptic investigation of particle precipitation dynamics for 60 substorms in IQSY (1964–1965) and IASY (1969), *Planet. Space Sci.*, *22*, 255–307, doi:10.1016/0032-0633(74)90028-2.

Brasseur, G., and S. Solomon (2005), *Aeronomy of the Middle Atmosphere*, 3rd ed., D. Reidel, Dordrecht, Netherlands.

Clilverd, M. A., C. J. Rodger, and T. Ulich (2006), The importance of atmospheric precipitation in storm-time relativistic electron flux drop outs, *Geophys. Res. Lett.*, *33*, L01102, doi:10.1029/2005GL024661.

Clilverd, M. A., C. J. Rodger, R. M. Millan, J. G. Sample, M. Kokorowski, M. P. McCarthy, T. Ulich, T. Raita, A. J. Kavanagh, and E. Spanswick (2007), Energetic particle precipitation into the middle atmosphere triggered by a coronal mass ejection, *J. Geophys. Res.*, *112*, A12206, doi:10.1029/2007JA012395.

Clilverd, M. A., et al. (2008), Energetic electron precipitation during substorm injection events: High-latitude fluxes and an unexpected midlatitude signature, *J. Geophys. Res.*, *113*, A10311, doi:10.1029/2008JA013220.

Clilverd, M. A., et al. (2009), Remote sensing space weather events: The AARDDVARK network, *Space Weather*, *7*, S04001, doi:10.1029/2008SW000412.

Clilverd, M. A., C. J. Rodger, R. J. Gamble, T. Ulich, T. Raita, A. Seppälä, J. C. Green, N. R. Thomson, J.-A. Sauvaud, and M. Parrot (2010), Ground-based estimates of outer radiation belt energetic electron precipitation fluxes into the atmosphere, *J. Geophys. Res.*, *115*, A12304, doi:10.1029/2010JA015638.

Clilverd, M. A., C. J. Rodger, I. J. Rae, J. B. Brundell, N. R. Thomson, N. Cobbett, P. T. Verronen, and F. W. Menk (2012), Combined THEMIS and ground-based observations of a pair of substorm associated electron precipitation events, *J. Geophys. Res.*, *117*, A02313, doi:10.1029/2011JA016933.

Connors, M., C. T. Russell, and V. Angelopoulos (2011), Magnetic flux transfer in the 5 April 2010 Galaxy 15 substorm: An unprecedented observation, *Ann. Geophys.*, *29*, 619–622, doi:10.5194/angeo-29-619-2011.

Erlandson, R. E., K. Mursula, and T. Bösinger (1996), Simultaneous ground-satellite observations of structured Pc 1 pulsations, *J. Geophys. Res.*, *101*(A12), 27,149–27,156, doi:10.1029/96JA02645.

Evans, D. S., and M. S. Greer (2004), Polar orbiting environmental satellite space environment monitor - 2: Instrument descriptions and archive data documentation, NOAA technical Memorandum, January 2004 version 1.4, Space Environ. Cent., Boulder, Colo.

Ferguson, J. A., and F. P. Snyder (1990), Computer programs for assessment of long wavelength radio communications, *Tech. Doc. 1773*, Natl. Ocean Syst. Cent., San Diego, Calif.

Fok, M.-C., R. B. Horne, N. P. Meredith, and S. A. Glauert (2008), Radiation Belt Environment Model: Application to space weather nowcasting, *J. Geophys. Res.*, *113*, A03S08, doi:10.1029/2007JA012558.

Fuselier, S. A., S. P. Gary, M. F. Thomsen, E. S. Claflin, B. Hubert, B. R. Sandel, and T. Immel (2004), Generation of transient dayside subauroral proton precipitation, *J. Geophys. Res.*, *109*, A12227, doi:10.1029/2004JA010393.

Hendry, A. T., C. J. Rodger, M. A. Clilverd, N. R. Thomson, S. K. Morley, and T. Raita (2012), Rapid radiation belt losses occurring during high-speed solar wind stream driven storms: Importance of energetic electron precipitation, in *Dynamics of the Earth's Radiation Belts and Inner Magnetosphere*, edited by D. Summers et al., AGU, Washington, D. C., in press.

Horne, R. B. (2002), The contribution of wave-particle interactions to electron loss and acceleration in the Earth's radiation belts during geomagnetic storms, in *Review of Radio Science 1999–2002*, edited by W. R. Stone, pp. 801–828, IEEE Press, Piscataway, N. J.

Horne, R. B., R. M. Thorne, S. A. Glauert, J. M. Albert, N. P. Meredith, and R. R. Anderson (2005), Timescale for radiation belt electron acceleration by whistler mode chorus waves, *J. Geophys. Res.*, *110*, A03225, doi:10.1029/2004JA010811.

Kangas, J., A. Aikio, and J. V. Olson (1986), Multistation correlation of ULF pulsations spectra associated with sudden impulses, *Planet. Space Sci.*, *34*, 543–553, doi:10.1016/0032-0633(86)90092-9.

Kennel, C. F., and H. E. Petschek (1966), Limit on stably trapped particle fluxes, *J. Geophys. Res.*, *71*, 1–28, doi:10.1029/JZ071i001p00001.

Lam, M. M., R. B. Horne, N. P. Meredith, S. A. Glauert, T. Moffat-Griffin, and J. C. Green (2010), Origin of energetic electron precipitation >30 keV into the atmosphere, *J. Geophys. Res.*, *115*, A00F08, doi:10.1029/2009JA014619.

Little, C. G., and H. Leinbach (1959), The riometer: A device for the continuous measurements of ionospheric absorption, *Proc. IRE*, *37*, 315–320.

Longden, N., M. H. Denton, and F. Honary (2008), Particle precipitation during ICME-driven and CIR-driven geomagnetic storms, *J. Geophys. Res.*, *113*, A06205, doi:10.1029/2007JA012752.

Miyoshi, Y., K. Sakaguchi, K. Shiokawa, D. Evans, J. Albert, M. Connors, and V. Jordanova (2008), Precipitation of radiation belt electrons by EMIC waves, observed from ground and space, *Geophys. Res. Lett.*, *35*, L23101, doi:10.1029/2008GL035727.

Ni, B., R. M. Thorne, Y. Y. Shprits, K. G. Orlova, and N. P. Meredith (2011), Chorus-driven resonant scattering of diffuse auroral electrons in nondipolar magnetic fields, *J. Geophys. Res.*, *116*, A06225, doi:10.1029/2011JA016453.

Onsager, T. G., R. Grubb, J. Kunches, L. Matheson, D. Speich, R. Zwickl, and H. Sauer (1996), Operational uses of the GOES energetic particle detectors, in GOES-8 and Beyond, *Proc. SPIE Int. Soc. Opt. Eng.*, *2812*, 281–290.

Randall, C. E., et al. (2005), Stratospheric effects of energetic particle precipitation in 2003–2004, *Geophys. Res. Lett.*, *32*, L05802, doi:10.1029/2004GL022003.

Reeves, G. D., et al. (2003), Acceleration and loss of relativistic electrons during geomagnetic storms, *Geophys. Res. Lett.*, *30*(10), 1529, doi:10.1029/2002GL016513.

Rodger, C. J., and M. A. Clilverd (2008), Magnetospheric physics: Hiss from the chorus, *Nature*, *452*(7183), 41–42, doi:10.1038/452041a.

Rodger, C. J., O. A. Molchanov, and N. R. Thomson (1998), Relaxation of transient ionization in the lower ionosphere, *J. Geophys. Res.*, *103*, 6969–6975, doi:10.1029/98JA00016.

Rodger, C. J., M. A. Clilverd, N. R. Thomson, R. J. Gamble, A. Seppälä, E. Turunen, N. P. Meredith, M. Parrot, J. A. Sauvaud, and J.-J. Berthelier (2007), Radiation belt electron precipitation into the atmosphere: Recovery from a geomagnetic storm, *J. Geophys. Res.*, *112*, A11307, doi:10.1029/2007JA012383.

Rodger, C. J., T. Raita, M. A. Clilverd, A. Seppälä, S. Dietrich, N. R. Thomson, and T. Ulich (2008), Observations of relativistic electron precipitation from the radiation belts driven by EMIC Waves, *Geophys. Res. Lett.*, *35*, L16106, doi:10.1029/2008GL034804.

Rodger, C. J., M. A. Clilverd, J. Green, and M.-M. Lam (2010a), Use of POES SEM-2 observations to examine radiation belt dynamics and energetic electron precipitation in to the atmosphere, *J. Geophys. Res.*, *115*, A04202, doi:10.1029/2008JA014023.

Rodger, C. J., M. A. Clilverd, A. Seppälä, N. R. Thomson, R. J. Gamble, M. Parrot, J.-A. Sauvaud, and T. Ulich (2010b), Radiation belt electron precipitation due to geomagnetic storms: Significance to middle atmosphere ozone chemistry, *J. Geophys. Res.*, *115*, A11320, doi:10.1029/2010JA015599.

Rodger, C. J., B. R. Carson, S. A. Cummer, R. J. Gamble, M. A. Clilverd, J.-A. Sauvaud, M. Parrot, J. C. Green, and J.-J. Berthelier (2010c), Contrasting the efficiency of radiation belt losses caused by ducted and non-ducted whistler-mode waves from ground-based transmitters, *J. Geophys. Res.*, *115*, A12208, doi:10.1029/2010JA015880.

Rodger, C. J., M. A. Clilverd, A. J. Kavanagh, C. E. J. Watt, P. T. Verronen, and T. Raita (2012), Contrasting the responses of three different ground-based instruments to energetic electron precipitation, *Radio Sci.*, *47*(2), RS2021, doi:10.1029/2011RS004971.

Seppälä, A., M. A. Clilverd, and C. J. Rodger (2007), NO_x enhancements in the middle atmosphere during 2003–2004 polar winter: Relative significance of solar proton events and the aurora as a source, *J. Geophys. Res.*, *112*, D23303, doi:10.1029/2006JD008326.

Seppälä, A., C. E. Randall, M. A. Clilverd, E. Rozanov, and C. J. Rodger (2009), Geomagnetic activity and polar surface level air temperature variability, *J. Geophys. Res.*, *114*, A10312, doi:10.1029/2008JA014029.

Smith, A. J. (1995), VELOX: A new VLF/ELF receiver in Antarctica for the Global Geospace Science mission, *J. Atmos. Terr. Phys.*, *57*, 507–524, doi:10.1016/0021-9169(94)00078-3.

Smith, A. J., R. B. Horne, and N. P. Meredith (2010), The statistics of natural ELF/VLF waves derived from a long continuous set of ground-based observations at high latitude, *J. Atmos. Sol. Terr. Phys.*, *72*, 463–475, doi:10.1016/j.jastp.2009.12.018.

Spann, J. F., M. Brittnacher, R. Elsen, G. A. Germany, and G. K. Parks (1998), Initial response and complex polar cap structures of the aurora in response to the January 10, 1997 magnetic cloud, *Geophys. Res. Lett.*, *25*, 2577–2580, doi:10.1029/98GL00647.

Spanswick, E., et al. (2009), Global observations of substorm injection region evolution: 27 August 2001, *Ann. Geophys.*, *27*, 2019–2025, doi:10.5194/angeo-27-2019-2009.

Summers, D., R. M. Thorne, and F. Xiao (1998), Relativistic theory of wave-particle resonant diffusion with application to electron acceleration in the magnetosphere, *J. Geophys. Res.*, *103*, 20,487–20,500, doi:10.1029/98JA01740.

Tsurutani, B. T., et al. (2001), Auroral zone dayside precipitation during magnetic storm initial phases, *J. Atmos. Sol. Terr. Phys.*, *63*, 513–522, doi:10.1016/S1364-6826(00)00161-9.

Turunen, E., P. T. Verronen, A. Seppälä, C. J. Rodger, M. A. Clilverd, J. Tamminen, C. F. Enell, and T. Ulich (2009), Impact of different precipitation energies on NO_x generation in the middle and upper atmosphere during geomagnetic storms, *J. Atmos. Sol. Terr. Phys.*, *71*, 1176–1189, doi:10.1016/j.jastp.2008.07.005.

Usanova, M. E., I. R. Mann, I. J. Rae, Z. C. Kale, V. Angelopoulos, J. W. Bonnell, K.-H. Glassmeier, H. U. Auster, and H. J. Singer (2008), Multipoint observations of magnetospheric compression-related EMIC Pc1 waves by THEMIS and CARISMA, *Geophys. Res. Lett.*, *35*, L17S25, doi:10.1029/2008GL034458.

Usanova, M. E., et al. (2010), Conjugate ground and multisatellite observations of compression-related EMIC Pc1 waves and associated proton precipitation, *J. Geophys. Res.*, *115*, A07208, doi:10.1029/2009JA014935.

Verronen, P. T., C. J. Rodger, M. A. Clilverd, and S. Wang (2011), First evidence of mesospheric hydroxyl response to electron precipitation from the radiation belts, *J. Geophys. Res.*, *116*, D07307, doi:10.1029/2010JD014965.

Xiao, F., R. M. Thorne, and D. Summers (2007), Higher-order gyroresonant acceleration of electrons by superluminous (AKR) wave-modes, *Planet. Space Sci.*, *55*, 1257, doi:10.1016/j.pss.2007.02.004.

Xiao, F., C. Shen, Y. Wang, H. Zheng, and S. Wang (2008), Energetic electron distributions fitted with a relativistic kappa-type function at geosynchronous orbit, *J. Geophys. Res.*, *113*, A05203, doi:10.1029/2007JA012903.

Xiao, F., Z. Su, H. Zheng, and S. Wang (2010), Three-dimensional simulations of outer radiation belt electron dynamics including cross-diffusion terms, *J. Geophys. Res.*, *115*, A05216, doi:10.1029/2009JA014541.

Xiao, F., S. Zhang, Z. Su, Z. He, and L. Tang (2012), Rapid acceleration of radiation belt energetic electrons by Z-mode waves, *Geophys. Res. Lett.*, *39*, L03103, doi:10.1029/2011GL050625.

Zhou, X.-Y., and B. T. Tsurutani (1999), Rapid intensification and propagation of the dayside aurora: Large-scale interplanetary pressure pulses (fast shocks), *Geophys. Res. Lett.*, *26*, 1097–1100, doi:10.1029/1999GL900173.

Zhou, X.-Y., R. J. Strangeway, P. C. Anderson, D. G. Sibeck, B. T. Tsurutani, G. Haerendel, H. U. Frey, and J. K. Arballo (2003), Shock aurora: FAST and DMSP observations, *J. Geophys. Res.*, *108*(A4), 8019, doi:10.1029/2002JA009701.